batteries

MDPI

Article

A Model for State-of-Health, Swelling and Out-of-Plane Stress Evolution in Lithium-Ion Batteries

Marios Mantelos *, Peter Gudmundson and Artem Kulachenko

Material and Structural Mechanics, Department of Engineering Mechanics, KTH Royal Institute of Technology, 100 44 Stockholm, Sweden; petergu@kth.se (P.G.); artem@kth.se (A.K.)
* Correspondence: mantelos@kth.se

Abstract

Module- and pack-level mechanical design of lithium-ion batteries in electric vehicles is a primary driver of swelling-induced stack pressure and spatially varying ageing. Current practice remains largely empirical or data-driven and configuration-specific, limiting the ability to predict how design changes translate into local pressure heterogeneity and state-of-health (SOH) loss. This motivates a compact chemo-mechanical model that maps packaging boundary conditions to pressure, swelling, and SOH evolution with few interpretable parameters. This study introduces finite-element-ready constitutive laws that couple reversible and irreversible swelling to SOH and through-thickness pressure, covering three boundary cases reported in literature: constant pressure, thickness clamp after an initial preload, and flexible support. Parameters are identified from different published datasets, and the model is validated against independent constraint scenarios. Good quantitative agreement is shown with averaged RMSE of 1.16% for SOH and 0.16 [MPa] for pressure evolution. Variance-based sensitivity analysis shows SOH uncertainty dominated by the damage-law parameters of the proposed constitutive relationship, whereas pressure evolution is primarily controlled by irreversible swelling and the non-linear through-thickness stiffness, indicating calibration priorities for engineering design studies. The framework is intended for fast comparative analyses of individual cells under a controlled environment. Further extensions, including SOC-dependent mechanics, refined hysteresis, temperature, and C-rate variations require dedicated datasets and are left for future work.

Keywords: lithium-ion batteries; state-of-health; reversible swelling; irreversible swelling; stack pressure; pouch cells; bracing; stiffness; constitutive modelling; pack design

Check for updates

Academic Editors: Wojciech Mrozik and Rodolfo Dufo-López

Received: 8 December 2025
Revised: 5 February 2026
Accepted: 21 February 2026
Published: 26 February 2026

Copyright: © 2026 by the authors. Licensee MDPI, Basel, Switzerland. This article is an open access article distributed under the terms and conditions of the Creative Commons Attribution (CC BY) license.

1. Introduction

There is an ongoing transition from fossil fuels toward electric vehicles powered by lithium-ion batteries, increasing the demand for improvements in lifetime, capacity retention, and cost efficiency. Predicting degradation and state-of-health (SOH) evolution, reversible and irreversible swelling, and stress evolution under realistic operating and packaging conditions is central to lifetime extension and robust design. Cell encapsulations into modules and packs introduce heterogeneous stress states and temperature fields that can drive spatially varying ageing and create weak spots that limit usable capacity even when most of the cell remains healthy [1,2]. Charge/discharge rate and temperature further affect capacity retention [3,4]. A predictive chemo-mechanical model therefore enables design evaluation of bracing, preload, and inter-cell pads with respect to spatial SOH evolution.

Mechanical boundary conditions are a decisive design variable in battery modules and packs [5–9]. During cycling, electrodes undergo reversible and irreversible swelling, and when this deformation is constrained by module bracing, inter-cell pads, and casing stiffness, it generates non-uniform stress fields and contact pressure distributions [10]. These pressure heterogeneities can locally alter chemical transport pathways and interfacial contact, and are thus associated with stress-induced ageing. This ageing manifests as capacity fade and impedance growth. This motivates an explicit chemo-mechanical framework that can translate packaging constraints into SOH evolution.

In parallel with these mechanical challenges, material research has focused on developing new composite electrodes to push the limits of energy and power. Recent examples include Fe_3O_4/reduced Graphene Oxide composite anodes [11,12] and scalable MXene ($Ti_3C_2T_x$) production routes aimed at next-generation Li-ion electrodes [13]. However, while such works motivate continued electrode innovation, large-scale industry use of such newer chemistries is still lacking. The primary objective is to resolve how mechanical boundary conditions couple to swelling, stress evolution, and SOH in full cells under conditions relevant to industrial battery integration. For that reason, the focus of the current work is on conventional/widely deployed oxide-graphite cell chemistries, which are the core of current markets and provide a better-characterised baseline that enables direct comparison with existing datasets. Aggregating data from multiple studies allows identification of constitutive models that persist across different cell configurations, providing confidence that the framework captures fundamental mechanical-degradation coupling rather than cell-specific behaviour.

The current state-of-the-art for optimizing module/pack design (bracing, preload, and pad compliance) in vehicle applications is mainly based on empirical testing. In recent years, data-driven methods for predicting SOH have advanced rapidly [14–18]. These methods, while powerful for predictions based on existing battery configurations, lack the mechanistic insight necessary to explore novel module or pack design changes and investigate constraint-driven heterogeneity.

Extensive work has examined microstructure and cracking evolution at the particle scale [19–21]. However, current chemo-mechanical models often fail to accurately link mechanical stresses and irreversible swelling to measurable SOH changes at the cell and module levels. Homogenisation models using representative volume elements capture stresses at the layer scale, including interactions between electrode particles [22,23]. Effects of lithium intercalation and the resulting reversible swelling on layer stress levels are also captured. These models, however, do not cover SOH evolution and irreversible swelling at cell and module scales. On an even larger scale, layer-level chemo-mechanical properties of the electrodes, current collectors and separators can be homogenised to obtain local battery properties [24]. The resulting homogenised properties represent the local average behaviour of a layered cell. Having the swelling history of electrode layers available, the resulting layer-level stresses can be calculated. While these techniques effectively represent average battery properties, they typically omit crucial local heterogeneities and thus are insufficient for detailed, position-specific predictions required for design optimization. Consequently, they cannot provide position-specific lifetime predictions of SOH and swelling evolution.

Unlike existing multiphysical [23,24] and purely data-driven battery models [14,15,25], the present framework couples the mechanical evolution of out-of-plane stresses and strains with a chemo-mechanical description of state-of-health (SOH) degradation. Many advanced models [19,26–29] treat small-scale phenomena (e.g., cracking of electrode particles) or rely on empirically calibrated electrochemical terms, but they often lack a means to directly simulate pressure-driven SOH evolution over large cells or modules. Based on the experimental works listed in Table 1 (digitisation process reported in the SI), this work

proposes a compact constitutive framework for rapid engineering-level assessment of how mechanical bracing and packaging constraints influence pressure evolution and state-of-health (SOH). The contribution is a finite-element-ready constitutive set that covers three boundary classes: constant pressure, thickness clamp after an initial pressure, and flexible support. The model assumes constant temperature and C-rate and adopts linear relations between damage and reversible/irreversible swelling. Detailed multiphysics couplings and chemistry/size-dependent nonlinearities are outside the present scope and left for future extensions.

Table 1. List of all the references used for parameter fit and/or validation of the model, including cell chemistry, nominal capacity and size.

Paper/Use	Cell Format	Chemistry	Capacity	Size
Li et al., 2019/Fit [30]	Large-format pouch	NMC111/ Graphite	24 [Ah]	200 mm × 150 mm × 7.7 mm
Cannarella & Arnold, 2014/Validation [31]	Pouch	LCO/ Graphite	500 [mAh]	25 mm × 35 mm × 6.5 mm
Aufschläger et al., 2024/Fit [32]	Pouch	NMC622/ Graphite	5 [Ah]	119 mm × 66 mm × 4.8 mm
Deich et al., 2021/Fit and Validation [7]	Large-format pouch	NMC622/ Graphite	60 [Ah]	322 mm × 97 mm × unreported

2. Experimental Observations and Theoretical Model

Several experimental studies of pouch cells subjected to repeated charging under various mechanical loading in terms of pressures have been presented in the literature. Here, only papers that consider constant temperature and charging conditions have been considered, as presented in the Section 1. This assumption is important, since temperature and C-rate modulate swelling kinetics, stress relaxation, and capacity fade, but current datasets under well-imposed boundary conditions seldom report the independent variation required to reliably identify these effects. Of particular interest is the evolution of state-of-health (SOH) and its dependence on number of charging cycles and mechanical pressure. Within this scope the results are promising, indicating that the proposed constitutive behaviour captures the mechanics-SOH coupling appropriately.

Three different mechanical loading conditions have been considered in the literature: 1. constant pressure [2,30,32–37], 2. initial pressure and subsequent thickness constraint [31,32,34,38–40], and 3. pouch cell connected by a mechanical stiffness and thickness constraint after application of the initial pressure [7,8,41,42]. These studies strongly emphasise that pressure has a significant influence on the evolution of SOH. The results from experimental investigations are presented graphically. Several studies present models that capture the experimental results [7,43–46]. However, an intuitive connection between the evolution of local and overall state-of-health, swelling, and internal stresses in battery layers, cells, and modules is currently missing. This paper presents a way forward based on the experimental observations presented in the literature.

The analysed experiments are one-dimensional from a mechanical modelling point of view. The mechanical state is described by a pressure p and a strain ε, defined as the thickness decrease divided by the initial thickness of the battery cell pack. It is emphasised that this definition of strain (positive for compression) is opposite in sign to the standard definition of strain, which is positive for tensile deformations.

In addition to strain caused by pressure p, the battery cell pack is swelling and shrinking during charge and discharge. The swelling strain can be divided into a reversible $\varepsilon_{\mathrm{rev}}$

and an irreversible contribution $\varepsilon_{\text{irrev}}$. Both are here defined as positive for corresponding thickness increases.

The reversible swelling strain is governed by lithium intercalation during a charge–discharge cycle and is cyclic, with a slowly varying amplitude dependent on the number of charging cycles. If the full charging range is considered, the reversible swelling strain can be described by the amplitude $\Delta\varepsilon_{\text{rev}} \geq 0$ that will depend on the number of charging cycles. In this way, the reversible swelling is defined as zero for discharged conditions and $\Delta\varepsilon_{\text{rev}}$ for fully charged conditions. The irreversible swelling strain $\varepsilon_{\text{irrev}}$ increases with the number of charging cycles.

Pressure p at fully charged conditions will depend on the mechanical strain ε_{m}, which is defined as the total strain ε, excluding the effects of swelling strains $\Delta\varepsilon_{\text{rev}}$ and $\varepsilon_{\text{irrev}}$.

$$\begin{aligned} \varepsilon_{\text{m}} &= \varepsilon + \Delta\varepsilon_{\text{rev}} + \varepsilon_{\text{irrev}} \\ p &= f(\varepsilon_{\text{m}}) \end{aligned} \tag{1}$$

The function f may be non-linear and history dependent. The influence of reversible and irreversible swelling strains is analogous to a thermal strain contribution, remembering the definition of positive directions for the strain variables. At discharged conditions, the term $\Delta\varepsilon_{\text{rev}}$ is set to zero in Equation (1).

To predict the pressure according to Equation (1), the evolution of reversible swelling strain amplitude $\Delta\varepsilon_{\text{rev}}$ and irreversible strain $\varepsilon_{\text{irrev}}$ is required. Beyond electrochemical conditions such as rate of charge and temperature, it can be assumed that they depend on pressure and state-of-health (SOH). In the present paper, SOH is defined as the ratio between current and initial charge capacity. Instead of SOH, a measure of total damage ω is used.

$$\omega = 1 - \text{SOH} \tag{2}$$

For given electrochemical conditions at charging/discharging, the evolution of reversible and irreversible strains will therefore depend on damage ω and pressure p. A complete description of all considered field variables also requires an evolution equation for the damage ω. In summary, the constitutive equations for the evolution of pressure, total strain, reversible swelling strain amplitude, irreversible swelling strain, and damage are governed by the mechanical stress–strain relation defined by Equation (1) and three evolution laws for $\Delta\varepsilon_{\text{rev}}$, $\varepsilon_{\text{irrev}}$, ω. Based on the experimental findings in the above-referenced papers, corresponding constitutive relationships are identified.

2.1. Reversible and Irreversible Swelling Strains

Evolution of reversible swelling as a function of the number of charging cycles is a cyclic function with a slowly varying amplitude. Measurements on pouch cells under constant pressure have been presented in [30,32,36]. Cannarella and Arnold, 2014 [31] present pressure amplitudes resulting from charging/discharging of pouch cells subjected to an initial pressure and then held at constant thickness. These pressure amplitudes result from reversible swelling. Based on the mechanical relationship between pressure and compression for the cells presented in the paper, the measured pressure amplitudes have been translated here into swelling amplitudes. A more detailed description is provided in the SI.

The references presented above consistently show a linear fit between reversible swelling strain amplitude $\Delta\varepsilon_{\text{rev}}$ and total damage $\omega = 1 - \text{SOH}$.

$$\Delta\varepsilon_{\text{rev}} = \Delta\varepsilon^{0}_{\text{rev}}(1 - q_{\text{rev}}\omega) \tag{3}$$

Here, $\Delta\varepsilon^0_{\text{rev}}$ denotes the initial reversible swelling strain amplitude for a fresh battery and q_{rev} a material constant. Experimental data are compiled in Figure 1 and yield slightly different parameter values. The variation is, however, rather small and can be attributed to the different types of tested pouch cells. Using linear regression, the values of $\Delta\varepsilon^0_{rev} \approx 1.88\%$ and $q_{rev} \approx 1.05$ are found. Detailed data identification from the papers used, digitisation, and subsequent conversions for use in the present manuscript are reported in the SI.

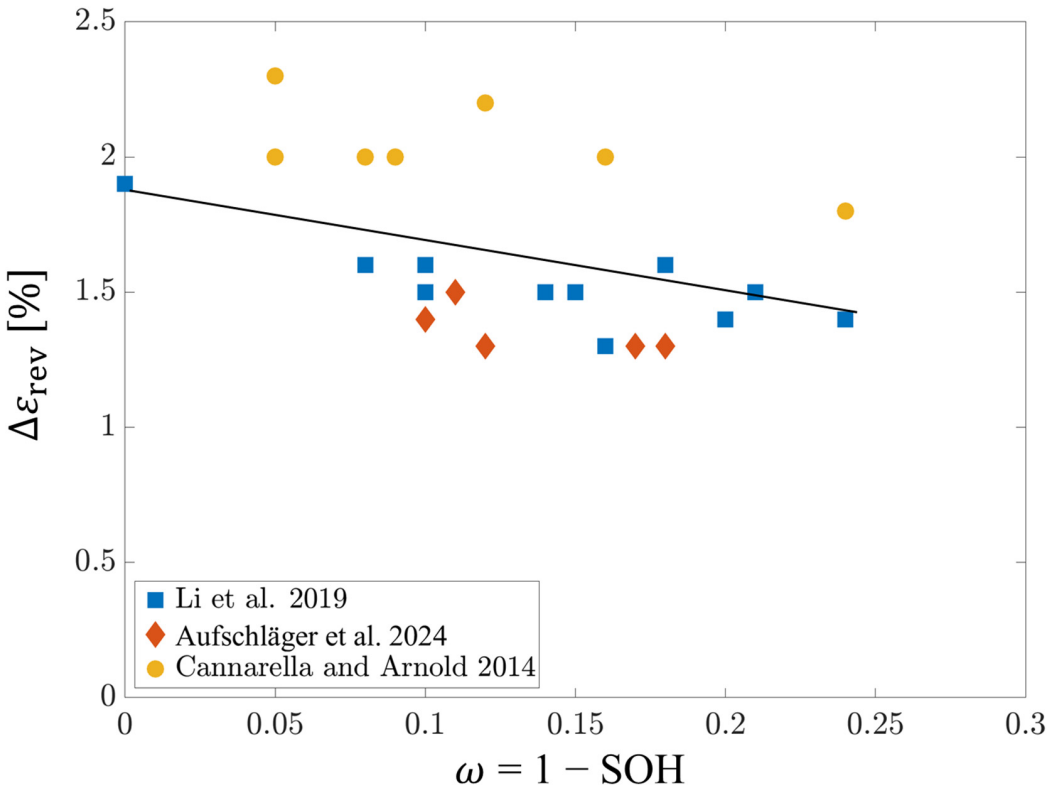


Figure 1. Reversible swelling strain amplitude versus damage $\omega = 1 - \text{SOH}$. Experimental results [30–32] and linear curve fit according to Equation (3).

Irreversible swelling strain has been measured in [2,8,32,36]. These studies indicate that $\varepsilon_{\text{irrev}}$ is approximately proportional to the damage ω. Irreversible strains often showcase a finite swelling $\varepsilon^0_{\text{irrev}}$ from the first so-called formation charging cycle due to the initial formation of SEI layers on fresh surfaces. Hence, if the formation cycle is considered, a reasonable model for irreversible strains can be formulated as,

$$\varepsilon_{\text{irrev}} = \varepsilon^0_{\text{irrev}} + q_{\text{irrev}}\omega \tag{4}$$

where $\varepsilon^0_{\text{irrev}}$ denotes the initial contribution from the first formation charging cycle and q_{irrev} is a material-dependent constant, reflecting the battery chemistry considered. From references [2,8,30,32,36] values for q_{irrev} in the range 0.1–0.5 are identified (detailed data identification from the related papers, digitisation, and subsequent conversions for use in the present manuscript are reported in the SI). A representable value for q_{irrev} equal to 0.3 is adopted in this work, with caution, as it reflects the approximate average derived from the manual compilation of data across multiple studies.

The relations in Equations (3) and (4) are motivated by physical/chemical mechanisms. Key degradation mechanisms causing loss of capacity (SOH) are the growth of solid-electrolyte-interphase (SEI), cracking of active particles, and lithium plating. Both SEI growth and lithium plating result in loss of lithium inventory (LLI) and induce irreversible swelling. Reduced lithium availability lowers intercalation, which decreases subsequent

reversible swelling. Furthermore, the cracking of active particles creates fresh surfaces that accelerate the total SEI growth. Cracking can also lead to electrochemically isolated sub-particles, causing the loss of electrode active material (LAM). Isolated sub-particles do not contribute to lithium intercalation, resulting in a reversible swelling decrease. Due to the release of particle residual stresses and the resulting deformations, cracking of active particles may also contribute to irreversible strain. Fully resolving these couplings in a computationally efficient, interpretable model of degradation, swelling, and stress evolution in battery modules and packs, is impractical as discussed further in Section 4. The linear relations used for reversible amplitude and irreversible swelling are pragmatic engineering approximations under constant conditions. They capture trends for moderate damage but do not reproduce late-stage "knee" behaviour reported for some chemistries. Where pronounced knees are expected, model predictions should be interpreted as local averages rather than detailed end-of-life dynamics.

2.2. Damage Evolution

Damage ω will increase with the number of charging cycles n. In applications, the number of charging cycles is on the order of 1000. Similar to fatigue crack growth in metals and damage evolution due to fatigue, the number of charging cycles n can be treated as a continuous dimensionless variable. A constitutive law for damage evolution can then be expressed in terms of $\frac{d\omega}{dn}$. Relevant experimental data have been reported in [2,7,31–33,41]. These results indicate that $\frac{d\omega}{dn}$ depends on the minimum and maximum pressure $p_{\min}$, $p_{\max}$ in the current charging cycle, as well as the current state of damage ω. Instead of minimum and maximum pressure, pressure dependence can be described in terms of $p_{\min}$ and $\Delta p = p_{\max} - p_{\min}$. Hence,

$$\frac{d\omega}{dn} = g(p_{\min}, \Delta p, \omega) \tag{5}$$

where $g(p_{\min}, \Delta p, \omega)$ is a function that must be experimentally determined for the battery system of interest. Here, a novel linear model is investigated. This simplified linear relationship represents experimentally observed phenomena clearly and directly, maintaining computational tractability while still embedding a clear mechanistic interpretation related to pressure-dependent degradation mechanisms. Hence,

$$\frac{d\omega}{dn} = q_1 + q_2 p_{\min} + q_3 \Delta p - q_4 \omega \tag{6}$$

where q_1, q_2, q_3, q_4 are material parameters. Predictions are intended for constant-condition scenarios or for comparative design studies where relative effects of mechanical constraints dominate, as stated in the Section 1.

The extensive experimental data presented by Deich et al., 2021 [7] have been analysed using Equation (6). Since $p_{\min} \approx 0$ in this investigation, the parameter q_2 does not appear in the model. The best fit for the other parameters is found as follows: $q_1 = 1.1 \times 10^{-4}$, $q_3 = 1.3 \times 10^{-4}$ [MPa^{-1}], $q_4 = 1.1 \times 10^{-3}$. (Detailed data identification from the related papers, digitisation, and subsequent conversions for use in the present manuscript are reported in Supplementary Materials). Predictions based on Equation (6) are compared to experimental data in Figure 2.

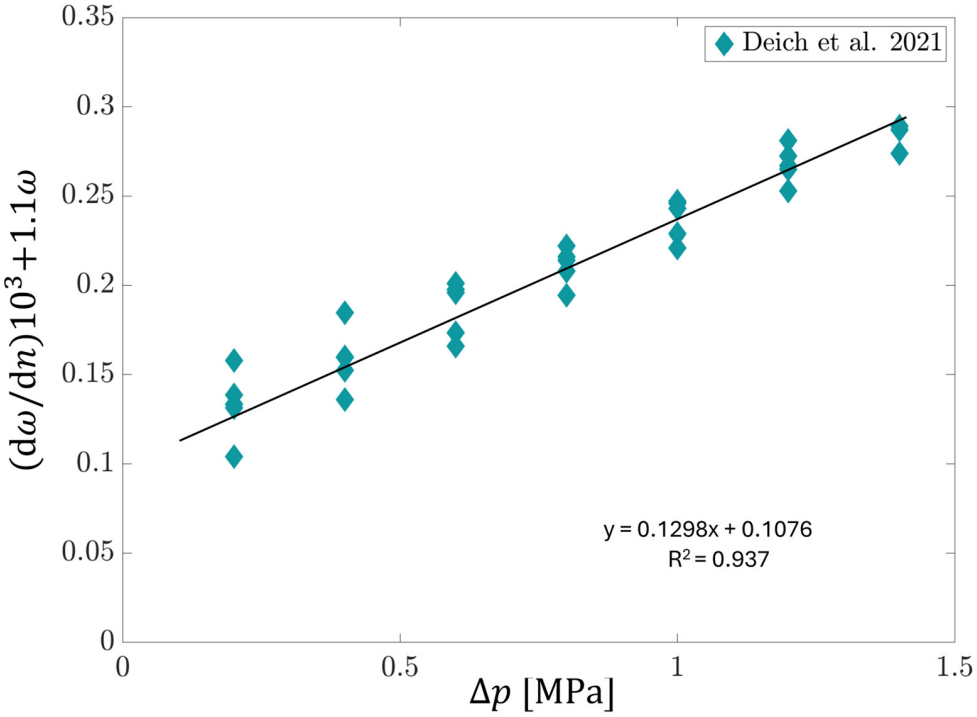


Figure 2. Comparison of experimental results from Deich et al. [7] and curve fit based on Equation (6).

2.3. Constitutive Law for Pressure-Compression

The relevant stiffness for pressure transmission is the stack-level through-thickness tangent stiffness, which differs from the in-plane electrode moduli due to progressive real contact area and layerwise compliance. The relationship between pressure p and compressive strain ε can be characterised by mechanical testing of pouch cells. Experimental data have been presented in [8,31,32,46,47]. They all exhibit non-linear behaviour with strong stiffening at larger strains, and Kong et al., 2025 [47] used the Ludwik isotropic hardening model to capture the response. Ludwik's power law inspires the presented approach. Swelling strains will depend on the mechanical strain ε_{m}, cf. Equation (1). A reasonable fit can be made as,

$$p = E_1\varepsilon_{\mathrm{m}} + E_3\varepsilon_{\mathrm{m}}^3 \tag{7}$$

Stiffness E_1 shows a small variation between the experiments, whereas E_3 varies between 1×10^4–4×10^4 [MPa]. Typical values for the parameters are $E_1 \approx 11$ [MPa], $E_3 \approx 2 \times 10^4$ [MPa]. The tangent stiffness E_{t} is determined as,

$$E_{\mathrm{t}} = \frac{dp}{d\varepsilon_m} = E_1 + 3E_3\varepsilon_{\mathrm{m}}^2 \tag{8}$$

In addition to the non-linear pressure–compressive strain relation during loading in Equation (7) several studies report a clear hysteresis effect upon unloading; see for example [8,46]. At the end of the first loading cycle, a permanent plastic compressive strain ε_{p} develops. Here, a simplified model for hysteresis and the corresponding plastic strain is applied, see Figure S1 in Supplementary Materials. Note that the plasticity presented here corresponds to swelling-induced strain associated with degradation, rather than classical stress-driven cyclic plasticity, thereby significantly reducing computational cost. The maximum experienced pressure during loading history up to the current state is denoted as $\overline{p}$. The corresponding mechanical strain $\bar{\varepsilon}_{\mathrm{m}}$ at this maximum pressure is determined from Equation (7). For pressures below $\overline{p}$, it is assumed that pressure–strain response is governed by the tangent stiffness E_{t} (Equation (8)) and a resulting plastic strain ε_{p}

defined in Equation (9) below. The constitutive model for pressure is therefore given by the following equations.

$$\varepsilon_p = \bar{\varepsilon}_m - \frac{\bar{p}}{E_t} \tag{9}$$

$$p = \begin{cases} E_1\varepsilon_m + E_3\varepsilon_m^3 & \varepsilon_m > \bar{\varepsilon} \\ E_t(\varepsilon_m - \varepsilon_p) & \varepsilon_p < \varepsilon_m \leq \bar{\varepsilon} \\ 0 & \varepsilon_m \leq \varepsilon_p \end{cases} \tag{10}$$

The constitutive law according to Equations (9) and (10) is also illustrated in the SI.

At a representative compressive strain of 0.03, Equation (8) yields a tangent out-of-plane stiffness of about 70 [MPa], far smaller than in-plane electrode stiffness measurements near 2 [GPa] for both anode and cathode layers [48,49]. One would expect comparable magnitudes in compression. The assembled pouch cell, however, exhibits a much smaller tangent stiffness. When considering the layered representation of the pouch cell, the current collectors Cu and Al (130 [GPa] and 70 [GPa], respectively) are far stiffer than 2 [GPa], and although the separator is soft, its small thickness limits its impact on the cell-level modulus. A plausible explanation for the low out-of-plane stiffness is related to imperfect contact conditions between layers. Electrode stacks are not perfectly flat but slightly wavy, so at low pressure only limited areas are in contact. As pressure rises, the real contact area grows, increasing the apparent out-of-plane stiffness. Furthermore, similar contact area evolution may occur at the scale of active particles. This phenomenon of low out-of-plane stiffness for layered structures has also been observed for packs of paper sheets [50].

3. Results

The application of the presented constitutive model expressed in Equations (3), (4) and (6)–(10) can now be applied to the different load cases presented in literature: 1. Constant pressure, 2. initial pressure and subsequent thickness constraint, and 3. pouch cell connected by a mechanical stiffness and thickness constraint after initial pressure. The coupled differential-algebraic equations for each case were all solved numerically in MATLAB R2024a using built-in ODE and DAE solvers. The fitted parameters presented in the figures above and also used in the following analyses are reported in Table 2.

Table 2. Fit model parameters for each validation case.

Parameter	Unit	Value ([7]/[31])	Notes
E_1	MPa	11	fixed
E_3	MPa	$2 \times 10^4 / 7 \times 10^3$	fitted
q_1	-	1.1×10^{-4} (Figure 2)	fitted
q_2	MPa^{-1}	0	fixed
q_3	MPa^{-1}	1.3×10^{-4} (Figure 2)	fitted
q_4	-	1.1×10^{-3} (Figure 2)	fixed
q_{rev}	-	1.05 (Figure 1)	fitted
q_{irrev}	-	0.3 (SI)	fitted
$\Delta\varepsilon_{rev}^0$	-	1.88%/2.50%	fitted

3.1. Constant Pressure

For a constant pressure p, the pressure amplitude term Δp disappears in Equation (6). The solution for damage growth as a function of the number of cycles is then determined as,

$$\omega = \frac{q_1 + q_2 p}{q_4}\left(1 - e^{-q_4 n}\right) \tag{11}$$

or equivalently in terms of state-of-health (SOH) as,

$$\mathrm{SOH} = 1 - \frac{q_1 + q_2 p}{q_4}\left(1 - e^{-q_4 n}\right) \tag{12}$$

According to the model, SOH will exponentially decrease and asymptotically reach a constant value of $1 - (q_1 + q_2 p)/q_4$. For small values of q_4 and/or the number of cycles n, SOH will linearly decay with n. The parameters in Equation (12) will, of course, depend on the battery composition. Comparisons can be made to experiments presented in the literature. Liu et al., 2013 [35] present a SOH evolution for vanishing pressure that largely agrees with the exponential decay expressed in Equation (12). Similarly, von Kessel et al., 2024 [51] present an exponentially decaying SOH for low-pressure levels. Wünsch et al., 2019 [42], de Sutter et al., 2020 [38], and Niu et al., 2021 [40] all report an approximately linear decay of SOH with number of cycles, indicating a small value of q_4 in Equation (12).

3.2. Initial Pressure and Thickness Constraint

In this case, a prescribed initial pressure p_0 is applied. The corresponding compressive strain ε_0 of the pouch cell can then be determined from Equation (7). This strain is subsequently kept constant. Reversible $\varepsilon_{\mathrm{rev}}$ and irreversible swelling strains $\varepsilon_{\mathrm{irrev}}$ will develop with number of cycles. The total strain ε is a superposition of swelling strains $\varepsilon_{\mathrm{rev}} + \varepsilon_{\mathrm{irrev}}$ and mechanical strain ε_{m}, $\varepsilon = \varepsilon_{\mathrm{m}} - (\varepsilon_{\mathrm{rev}} + \varepsilon_{\mathrm{irrev}})$. Note that the swelling strains are defined as positive for thickness increases, whereas the mechanical and total strain are defined as positive for compressive strains (negative strains). The pressure is given by the mechanical strain ε_{m} through Equations (9) and (10) with $\varepsilon_{\mathrm{m}} = \varepsilon + \varepsilon_{\mathrm{rev}} + \varepsilon_{\mathrm{irrev}}$. The evolution of ω, p, $\Delta\varepsilon_{\mathrm{rev}}$, $\varepsilon_{\mathrm{irrev}}$ is obtained by the solution of Equations (3), (4), (6), (9) and (10). At a given state in terms of number of cycles n, the maximum pressure p_{max}, minimum pressure p_{min}, and resulting pressure amplitude, $\Delta p = p_{\mathrm{max}} - p_{\mathrm{min}}$, for a charging–discharging cycle are determined from Equations (9) and (10) applying $\varepsilon_{\mathrm{rev}} = \Delta\varepsilon_{\mathrm{rev}}$ and $\varepsilon_{\mathrm{rev}} = 0$, respectively.

Comparisons are made with the experimental results reported by Cannarella and Arnold, 2014 [31]. Fitting the reported pressure–compressive strain data presented in the paper yields $E_1 = 11$ [MPa], $E_3 \approx 7 \times 10^3$ [MPa] according to Equation (7). The initial reversible strain amplitude $\Delta\varepsilon_{\mathrm{rev}}^0$ was also estimated from [31] to be 2.5%. Furthermore, the initial irreversible strain was assumed to vanish. The parameters q_{rev}, q_{irrev}, q_1, q_3, q_4 were taken from the typical values presented in Sections 2.1 and 2.2. The parameter q_2 was assumed to vanish. All the parameter values are summarised in Table 2. In Figure 3, the predicted evolution of state-of-health and maximum pressure with number of charging cycles is compared to the experimental results for the "medium" pressure case presented in [31]. Even though not all parameters can be determined from [31], the agreement between simulations and experimental data is very good. The root-mean-squared-error (RMSE) is the quadratic mean of the differences between prediction and experiment, and are reported, for this comparison, as $\mathrm{RMSE}_{\mathrm{SOH}}$ = 1.12% and $\mathrm{RMSE}_{\mathrm{P}}$ = 0.03 [MPa].

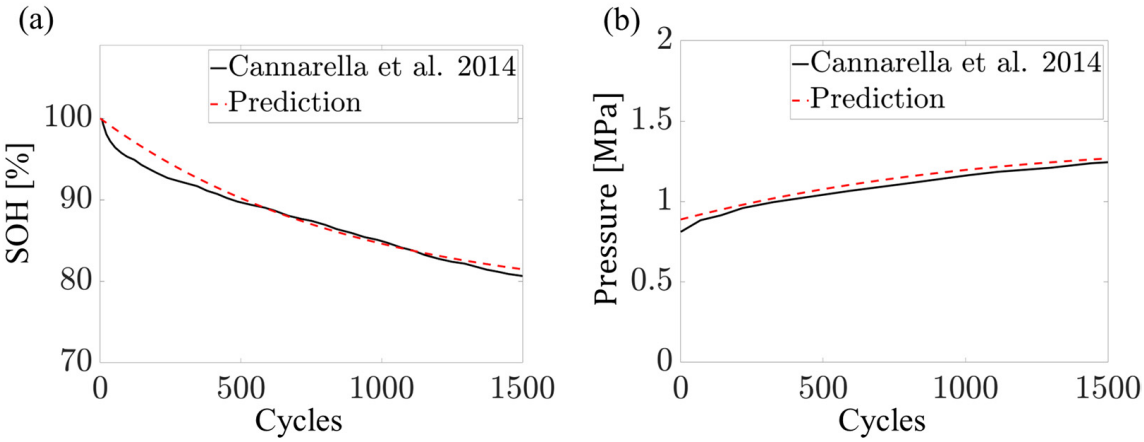


Figure 3. Comparisons between predictions and experiments [31] for the evolution of the state-of-health (**a**) and pressure (**b**) versus number of charging cycles.

3.3. Initial Pressure and Flexible Support

Experiments have been conducted for a pouch cell in series or parallel with an elastic stiffness. In this way, the effects of flexible encapsulations and tabs between battery cells can be simulated. Michelini et al., 2023 [41] and Wünsch et al., 2019 [42] have investigated a pouch cell that is mechanically connected to a stiffness in series. A simplified illustration is provided in Figure S2 of the Supplementary Materials. An initial pressure p_0 is applied, leading to a total compression (displacement) u_0 of the combined pouch cell and elastic stiffness. This compression is then kept constant during the subsequent charging cycles. The initial pressure p_0 defines the initial mechanical compressive strain ε_0 of the pouch cell according to Equation (7) and the compressive deformation u_s of the elastic stiffness is given by $u_s = p/k$ where k is the stiffness coefficient [MPa/mm]. Initially,

$$u_0 = p_0/k + t\varepsilon_0 \tag{13}$$

where t is the thickness of the pouch cell.

At a given state in terms of the number of cycles n and swelling strains $(\Delta\varepsilon_{rev}, \varepsilon_{irrev})$, the maximum pressure $p = p_{min} + \Delta p$ at fully charged conditions and the corresponding battery strain ε are found from,

$$\begin{aligned} u_0 &= p/k + t\varepsilon \\ \varepsilon_m &= \varepsilon + \Delta\varepsilon_{rev} + \varepsilon_{irrev} \end{aligned} \tag{14}$$

together with the constitutive equation defined in Equations (9) and (10). The minimum pressure p_{min} is similarly determined from Equations (9), (10) and (14) with $\Delta\varepsilon_{rev} = 0$. The evolution equations for reversible strain amplitude $\Delta\varepsilon_{rev}$, irreversible strain ε_{irrev} and damage ω (state-of-health) follow from Equations (3), (4) and (6).

Deich et al., 2021 [7] and Hahn et al., 2021 [8] use an experimental setup in which the pouch cell and a mechanical stiffness are coupled in parallel. A simplified illustration is provided in the SI. In [7], the cell alone is first subjected to an initial pressure p_{init}, which results in a cell compression ε_{init} according to Equation (7). The mechanical stiffness k is then applied in parallel and subsequently, the initial pressure p_{init} is removed. The condition of vanishing total force for the pouch cell and mechanical stiffness in parallel is expressed by,

$$0 = kt(\varepsilon_0 - \varepsilon_{init}) + p_0 \tag{15}$$

where k denotes the mechanical stiffness [MPa/mm], t the thickness of the cell, p_0 the pressure, and ε_0 the resulting compressive strain of the cell. Using Equations (9) and (10),

the compression of the cell ε_0 and pressure p_0 can now be determined. At subsequent charging, the strain ε_0 and pressure p_0 in Equation (15) are replaced by the current values ε, p, respectively. Equations (13) and (14) are recovered if u_0 is identified as $t\varepsilon_{\text{init}}$. Hence, the two setups, spring and cell in series or in parallel, are equivalent from a simulation point of view. Deich et al., 2021 [7] present measurements of state-of-health and pressure as functions of number of charging cycles for nine different combinations of initial pressures p_{init} and mechanical stiffnesses k, see Table 1. It is evident that these parameters strongly influence SOH and pressure. Comparisons are made with simulations using the present model. In the simulations, typical values for parameters $\Delta\varepsilon^0_{\text{rev}}$, q_{rev}, q_{irrev}, q_1, q_3, q_4, E_1, E_3 as presented in Sections 2.1–2.3 are used. The parameters q_2 and $\varepsilon^0_{\text{irrev}}$ are neglected. It should be noted that except for parameters q_1, q_3, q_4, the remaining parameter values are taken from data based on other publications; see Sections 2.1 and 2.2 and Table 2. A thickness of t = 10.4 mm for the cells was identified from information in [7].

The results for state-of-health and maximum pressure evolutions as functions of number of charging cycles are presented in Figures 4 and 5 and are discussed in Section 4. The results are encouraging, and RMSEs are reported in Table 3. The model reproduces the observed trends and magnitudes across varying initial pressures and stiffnesses with good accuracy.

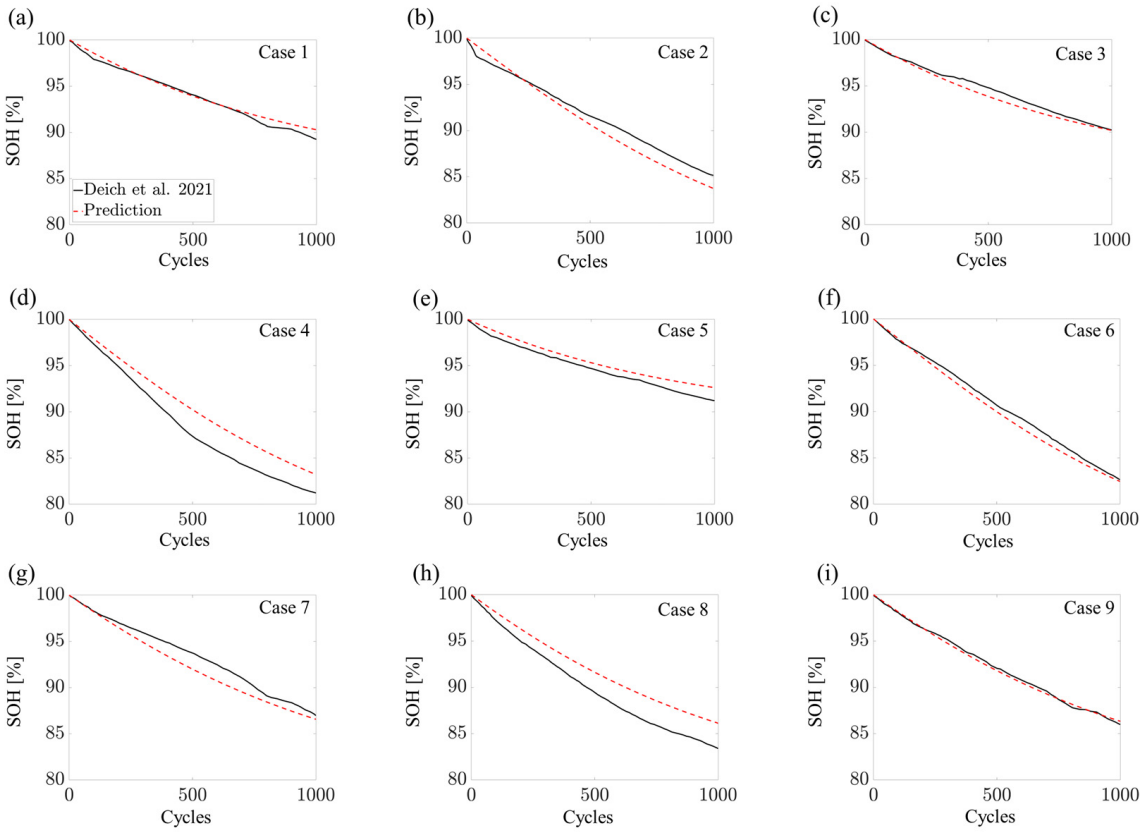


Figure 4. Comparison between experiments (solid lines) [7] and simulations (dashed lines) for the state-of-health evolution with the number of charging cycles. The diagrams represent different combinations of initial pressure and mechanical stiffness according to Table 3. (**a**) Case 1 with k = 3.20 [MPa/mm] and p_{init} = 25.00 [kPa]; (**b**) Case 2 with k = 16.00 [MPa/mm] and p_{init} = 25.00 [kPa]; (**c**) Case 3 with k = 3.20 [MPa/mm] and p_{init} = 65.00 [kPa]; (**d**) Case 4 with k = 16.00 [MPa/mm] and p_{init} = 65.00 [kPa]; (**e**) Case 5 with k = 0.55 [MPa/mm] and p_{init} = 45.00 [kPa]; (**f**) Case 6 with k = 18.60 [MPa/mm] and p_{init} = 45.00 [kPa]; (**g**) Case 7 with k = 9.60 [MPa/mm] and p_{init} = 16.70 [kPa]; (**h**) Case 8 with k = 9.60 [MPa/mm] and p_{init} = 73.30 [kPa]; (**i**) Case 9 with k = 9.60 [MPa/mm] and p_{init} = 45.00 [kPa].

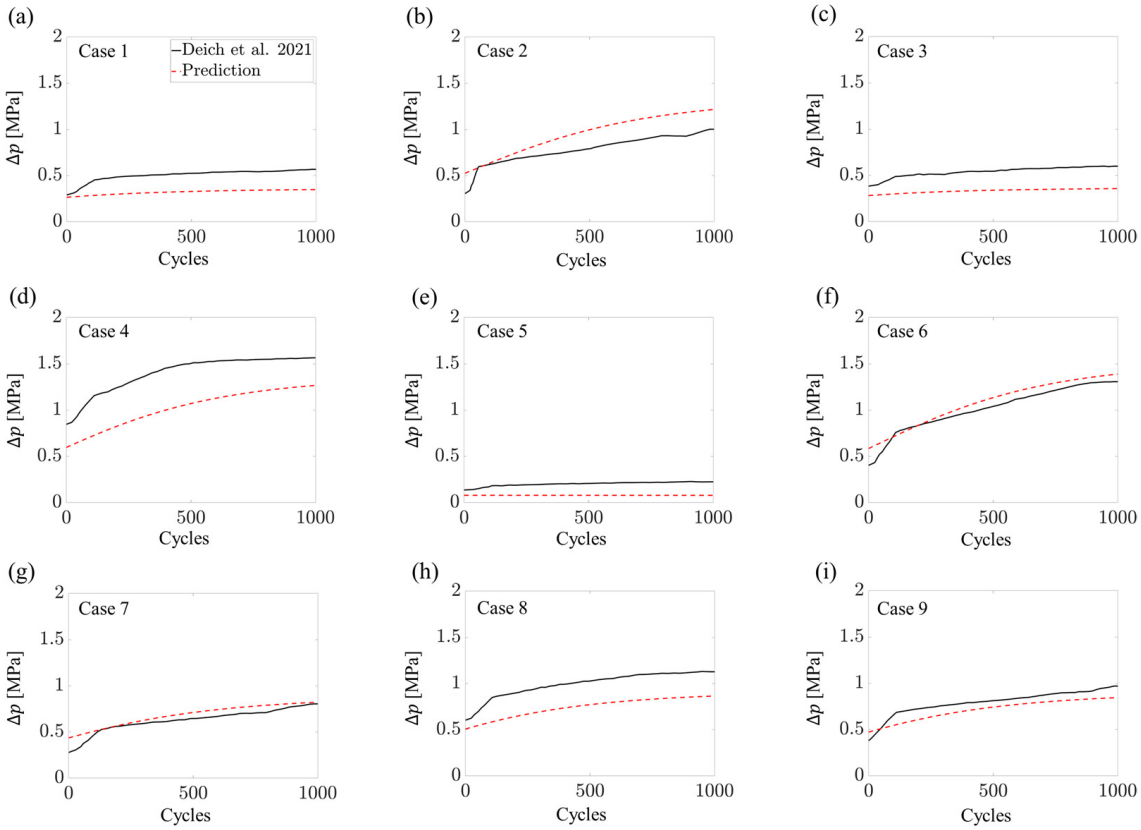


Figure 5. Comparison between experiments (solid lines) [7] and simulations (dashed lines) for maximum pressure evolution with number of charging cycles. The diagrams represent different combinations of initial pressure and mechanical stiffness according to Table 3. (**a**) Case 1 with k = 3.20 [MPa/mm] and p_{init} = 25.00 [kPa]; (**b**) Case 2 with k = 16.00 [MPa/mm] and p_{init} = 25.00 [kPa]; (**c**) Case 3 with k = 3.20 [MPa/mm] and p_{init} = 65.00 [kPa]; (**d**) Case 4 with k = 16.00 [MPa/mm] and p_{init} = 65.00 [kPa]; (**e**) Case 5 with k = 0.55 [MPa/mm] and p_{init} = 45.00 [kPa]; (**f**) Case 6 with k = 18.60 [MPa/mm] and p_{init} = 45.00 [kPa]; (**g**) Case 7 with k = 9.60 [MPa/mm] and p_{init} = 16.70 [kPa]; (**h**) Case 8 with k = 9.60 [MPa/mm] and p_{init} = 73.30 [kPa]; (**i**) Case 9 with k = 9.60 [MPa/mm] and p_{init} = 45.00 [kPa].

Table 3. Nine different test cases with different combinations of initial pressures and mechanical stiffnesses [7]. The letters refer to the cases presented in Section 4.

Case	k [MPa/mm]	p_{init} [kPa]	RMSE_{SOH} [%]	$\text{RMSE}_{\Delta P}$ [MPa]
1(a)	3.20	25.00	0.75	0.18
2(b)	16.00	25.00	0.51	0.18
3(c)	3.20	65.00	0.35	0.21
4(d)	16.00	65.00	3.13	0.38
5(e)	0.55	45.00	0.91	0.12
6(f)	18.60	45.00	0.75	0.08
7(g)	9.60	16.70	0.54	0.06
8(h)	9.60	73.30	2.79	0.25
9(i)	9.60	45.00	0.73	0.09

3.4. Sensitivity Analysis and Parameter Influence

The influence of the model parameters uncertainty on the quantities of interest (SOH and pressure evolution) was quantified using variance-based global sensitivity analysis (Sobol indices). The chosen scalar quantities of interest are the final SOH, P_{end}, ΔP_{end}, in accordance with the validation results presented in Figures 3–5. Parameters were uniformly distributed $\pm 10\%$ of their nominal values. For each quantity of interest, the total-order indices $S_{\text{t,i}}$ are reported, which represent the fraction of the output variance attributed to a parameter i including all interaction effects. This means that parameters with large $S_{\text{t,i}}$ are the dominant drivers of output uncertainty and, thus, are the highest priority targets for improved characterization or calibration. The sampling process was based on quasi-random Sobol sequences, and the total-order indices were calculated using the Jansen estimator, as described in [52]; 95% confidence intervals were obtained by bootstrap resampling (200 replicates).

The Sobol base sample size N was selected after a convergence study. Using a fixed sampling sequence, $S_{\text{t,i}}$ were recomputed for nested prefixes $512 \leq \text{N} \leq 5120$, and the maximum change between successive N was monitored. For the SOH analyses, a noticeable correction occurred between N = 1024 and N = 2048, while changes for $\text{N} \geq 4096$ were below 0.03. For the pressure-based analyses, convergence was smoother and changes decreased below 0.03 by N = 4096. Therefore, for all the reported analyses, N = 4096 was used as the smallest value, yielding stable total-order index estimates. The results show different high sensitivity based on the quantities of interest. When comparing against SOH Figure 6a,b at the last cycle, the damage parameters q_1, q_3, q_4 are the most sensitive. This effect stems from the individual terms of Equation (6). The connection of q_3 with ΔP also showcases the dependency on the rest of the parameters via Equations (6)–(8) and (10). Differences between the two cases (a) and (b) result from the different boundary conditions applied both experimentally and computationally. In Figure 6c,d, where the quantity of interest is pressure evolution, higher sensitivity is showcased by q_{irrev} and E_3. The dominant sensitivity to q_{irrev} indicates that uncertainty propagation is controlled primarily by irreversible deformation, consistent with the intent of the formulation and literature linking pressure build-up to irreversible swelling under mechanical constraints. The lower uncertainty of the other parameters stems from the damage evolution expression. It is evident that E_1 has a negligible effect and is thus considered non-influential within the tested $\pm 10\%$ range. The magnitude of E_1 is much smaller than E_3, and combined with the mechanical strain mainly affects the initial pressure evolution. In addition, as stated in Section 2.3, this initial response is described by values of E_1 with small variation. Towards EOL (end-of-life), where the analysis quantities of interest are selected, that evolution is mostly affected by E_3 and irreversible strains. However, it is kept in the formulation to intentionally make it more open to future inclusions of various new chemistries, whose initial behaviour may be more unstable.

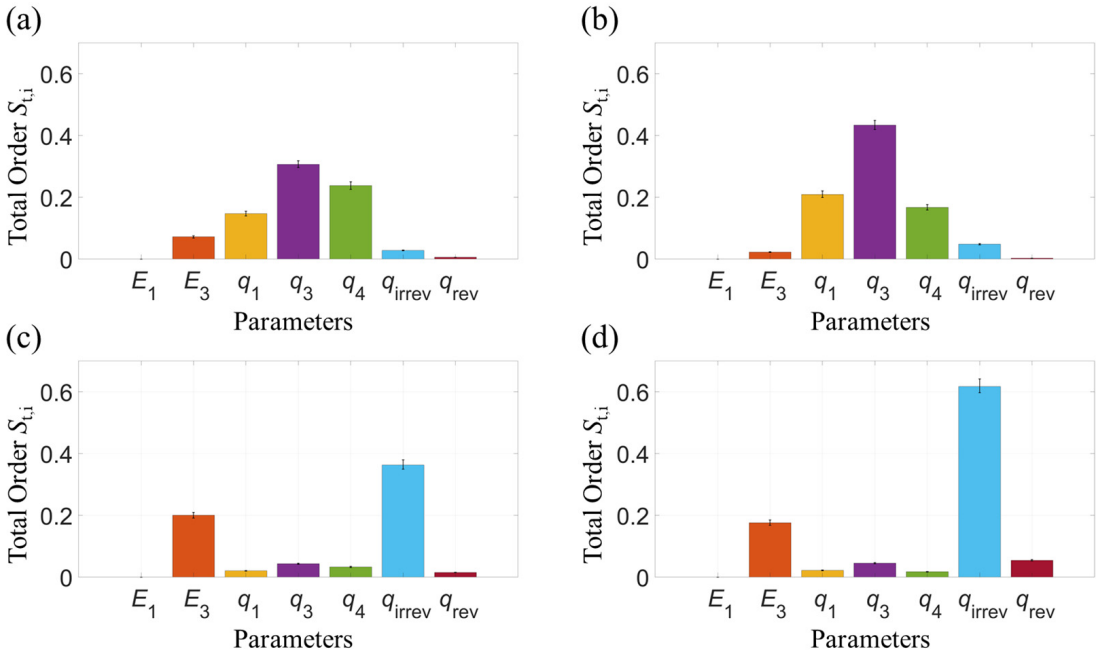


Figure 6. Total-order Sobol indices $S_{t,i}$ for (**a**) SOH for Cannarella and Arnold, 2014 [31] (**b**) SOH for Deich et al., 2021 [7], (**c**) P_{end} for Cannarella and Arnold, 2014 [31], and (**d**) ΔP_{end} Deich et al., 2021 [7] in accordance with the validation results. Bars show the total order Sobol index $S_{t,i}$ and whiskers indicate 95% confidence intervals.

4. Discussion

The comparisons between experiments and simulations for the state-of-health and pressure evolutions presented in Figures 3–5 are encouraging for further development. Despite several parameters for swelling and SOH evolution being estimated from prior studies, good agreement is obtained. Determining all the parameters for a particular battery cell under these different mechanical loading conditions would result in a more accurate representation from the current model.

The results presented in Figure 4 and RMSEs reported in Table 3 show that state-of-health is well predicted for the different mechanical support conditions. The influence of the support stiffness k at constant initial pressure p_{init} is evident when comparing Figure 4a,c,e with Figure 4b,d,f, respectively. The detrimental effect of increasing stiffness is well captured by the model. Similarly, the effect of initial pressure p_{init} at constant support stiffness k is observed when Figure 4a,b,g are compared to Figure 4c,d,h, respectively. The effect is more pronounced in the experimental results compared to the corresponding simulations, and further discussion on this matter is following later.

Several studies report a non-monotonic dependence of ageing on stack pressure, with a beneficial or optimal pressure window rather than strictly monotonic behaviour [31,32,53]. The present model does not reproduce such a window because under constant pressure loading, Equation (11) shows a monotonic damage reduction with decreasing pressure. Capturing an optimum at non-zero pressure would require a modified dependence in Equation (6), a convex or saturating contribution of p_{min}, which cannot be uniquely identified from the available datasets and is therefore omitted here.

For the flexible support cases, the model captures the overall pressure trends, as can be seen in Figure 5, but early cycle discrepancies remain. In particular, the "knee" around 100 cycles in [7] is likely influenced by the experimental protocol. The initial loading was conducted at 30% SOC, while reported maxima beyond 100 cycles were measured at 100-cycle intervals and correspond to 100% SOC. In the present simulations, pressure curves are held at 100% SOC throughout, which can bias the initial peak and introduce

knees. Incorporating SOC-dependent mechanical response and time-dependent relaxation (viscoelastic contribution) would reduce the early cycle offset.

More generally, the pressure evolution law in Equations (9) and (10) provides a simplified representation of unloading hysteresis, and as stated previously, does not include viscous stress relaxation. In particular, the hysteresis behaviour is, in reality, more complex [8,46]. The unloading path is not simply linear. Nevertheless, the simplified model captures SOH and pressure evolution. These simplifications are intentional to keep the framework compact and readily implementable in the finite element method. At the same time, extending the model is presently constrained by data availability: most published datasets do not independently vary temperature, C-rate, and hold times under well-defined mechanical boundary conditions, which prevents reliable separation and calibration of these contributions. However, they define the rate of applicability. Predictions are most reliable for cycling at fixed temperature and C-rate, and at this stage, should not be extrapolated to pack environments with gradients. Extending the framework would require (a) dedicated loading-unloading measurements across relevant SOC windows to define a more realistic unloading path, (b) experiments with hold segments to identify relaxation and (c) datasets with independent variations of temperature and C-rate to identify parameter scaling.

Although explicit electrochemical modelling could improve accuracy and make the study more chemistry-specific, it substantially increases complexity and computational cost. The current formulation deliberately avoids direct electrochemical terms, capturing their net effects via experimentally validated constitutive parameters. This approach retains critical mechanistic insights without sacrificing computational simplicity, making it particularly suitable for iterative design optimisation processes, as summarised in Table 4, which compares the proposed model with relevant approaches from literature.

A key advantage is that within this linear, constant-condition framework, qualitative parameter influences can be stated explicitly without further computation. A higher damage-rate intercept in Equation (6) reduces the number of cycles to a given SOH threshold. A higher mean-pressure coefficient increases the degradation rate under constant-pressure and thickness-clamp conditions, with a stronger effect when pressure transients are larger. A higher initial reversible amplitude enlarges the pressure-oscillation envelope under flexible support. The tangent stiffness of the pressure-compression relation governs the translation between compression and pressure; a higher tangent stiffness at the operating compression level amplifies the pressure swing for a given swelling amplitude. These tendencies, clearly summarised in the sensitivity analysis section, indicate calibration priorities for engineering use.

The substantial difference in in-plane and out-of-plane stiffnesses discussed in Section 2.3 affects stresses resulting from intercalation swelling of active particles. For example, an active layer swelling of 2% yields in-plane stresses on the order of 40 [MPa], whereas the out-of-plane pressure reaches only around 1 [MPa]. Hence, local stresses within active layers are mainly controlled by in-plane components. Stress-controlled damage evolution within electrode layers will, therefore, be determined by the evolution of in-plane stresses. This seems to contradict the effect of (out-of-plane) pressure on the state-of-health evolution presented in the paper. One explanation could be that the pressure influences the evolution of surface-related damage between layers. Inhomogeneous contact conditions between layers may lead to locally high contact pressures in smaller areas and vanishing pressure in areas that are not in contact. This can result in surface-related damage, such as lithium plating. Further research is required to investigate damage mechanisms in more detail.

Table 4. Comparison of the presented model to relevant works from literature [7,15].

Aspect	This Work	Deich et al., 2021 [7]	Zhu et al., 2022 [15]
Boundary conditions covered	Constant pressure; thickness clamp after initial pressure; flexible support	Flexible support	None
Parameter count	Few; directly interpretable	Few directly interpretable; uncertainty in fatigue parameters	Many; statistical parameters from the experimental curves; trained weights and biases
Temperature/C-rate	Constant	Constant	Varying (Different temperature (25 °C, 35 °C, 45 °C) and charge/discharge rate (0.25/1, 0.5/1, 1/1, 0.5/1, 0.5/2, 0.5/4) combinations. Zhu et al. showed that in ambient temperature, capacity fade is not affected by the C-rates variation. In constant charge–discharge rate conditions, cycling in 35 °C improved the total lifetime of the cell)
Computational cost	Very low; FE-ready	Low; needs extension for FE coupling	Very low after the collection of the voltage relaxation data
Primary use case	Pack-level bracing and design optimization studies	Module design optimization	On-board SOH prediction

The presented constitutive model can be implemented in a finite element program to simulate local state-of-health, swelling, and pressure evolution in battery cells, modules, and packs as a function of the number of charging cycles. One way is to homogenise battery properties using laminate theory models [24]. The in-plane constitutive behaviour can be modelled by laminate theory, and the current model can represent the out-of-plane properties. This coupling with the homogenisation scheme enables fast cell, module-, and pack-level simulations that can be used iteratively for design, casing, and bracing optimisation. It would also enable size-specific cell investigation. Work in this direction is ongoing, and results will be presented in future publications.

5. Conclusions

This study presents a computationally efficient constitutive framework for predicting the coupled evolution of state-of-health, swelling, and mechanical stresses in lithium-ion battery cells under various mechanical constraints. The model successfully captures

experimental trends across three distinct boundary conditions: constant pressure, thickness constraint following initial compression, and flexible support configurations. Validation against independent experimental datasets demonstrates an averaged RMSE of 1.16% for state-of-health evolution and 0.16 [MPa] for pressure development.

The model requires eight material parameters that can be determined from standard mechanical testing and cycling experiments. Calibration for specific cells (chemistry, size) under a specific mechanical boundary condition requires a single multiple-cycle experiment with simultaneous monitoring of pressure, strain, reversible, and irreversible swelling, and capacity with respect to the number of cycles. This represents a modest experimental investment compared to full design-of-experiments approaches. Practical applications of the model include optimization of module-level bracing systems, evaluation of thermal pad stiffness effects on battery lifetime, and assessment of packaging constraints in vehicle integration. The framework enables quantitative comparison of different mechanical support strategies during the design phase. Implementation in finite element software is straightforward due to the explicit algebraic form of the constitutive equations, allowing three-dimensional simulations of heterogeneous stress and state-of-health distributions within battery packs.

This framework is intended for comparative design studies under controlled cycling conditions and captures average SOH, pressure and swelling trends under the three mechanical conditions considered. Extension to variable temperature/C-rate operations, refined unloading/hysteresis, and time-dependent stress relaxation require targeted datasets of the type outlined above and are left for future work.

Supplementary Materials: The following supporting information can be downloaded at: https://www.mdpi.com/article/10.3390/batteries12030081/s1. Details on external data sources and digitisation/conversion procedures used for parameter fitting and validation; extraction of irreversible strain parameters; additional illustrative figures (Figure S1: Pressure evolution illustration using our constitutive law with the fitted values from Deich et al. and illustration of the unloading path; Figure S2: Illustration of different experimental boundary constraint equivalents: (a) spring in series with the cell, (b) spring in parallel with the cell).

Author Contributions: M.M.: Data curation, Formal analysis, Investigation, Software, Validation, Writing—original draft, Writing, Review and editing, P.G.: Conceptualisation, Data curation, Formal analysis, Funding acquisition, Investigation, Methodology, Validation, Writing—original draft, Writing, Review and editing, A.K.: Formal analysis, Funding acquisition, Software, Validation, Writing, Review and editing. All authors have read and agreed to the published version of the manuscript.

Funding: The financial support from the Swedish Energy Agency under contract P2023-00090 is gratefully acknowledged.

Data Availability Statement: The original data presented in the study are openly available in repository PaperStateOfHealth at https://github.com/mar3mad/PaperStateOfHealth (accessed on 15 December 2025).

Conflicts of Interest: The authors declare no conflicts of interest.

Abbreviations

The following abbreviations are used in this manuscript:

SOH	State-of-health
SOC	State-of-charge
SEI	Solid-electrolyte interphase
LLI	Loss of lithium inventory
LAM	Loss of active material

FE	Finite element
RVE	Representative volume element
DAE	Differential-algebraic equation
ODE	Ordinary differential equation
ε_{irrev}	Irreversible swelling strain
ε_{rev}	Reversible swelling strain
ε_{m}	Mechanical strain, positive for compression
$\Delta\varepsilon_{rev}$	Reversible strain amplitude
$\Delta\varepsilon_{rev}{}^{0}$	Initial reversible strain amplitude
$\varepsilon_{irrev}{}^{0}$	Initial irreversible strain contribution from formation cycle
p_{min}	Minimum pressure
p_{max}	Maximum pressure
$S_{t,i}$	Total order Sobol index
RMSE	Root-mean-squared-error

References

1. Park, K.; Lee, M.; Song, J.; Ha, A.R.; Ha, S.; Jo, S.; Song, J.; Choi, S.H.; Kim, W.; Ryu, K.; et al. Operando Spatial Pressure Mapping Analysis for Prototype Lithium Metal Pouch Cells Under Practical Conditions. *Adv. Sci.* **2023**, *10*, 2304979. [CrossRef]
2. Li, R.; Ren, D.; Wang, S.; Xie, S.; Hou, Z.; Lu, L.; Ouyang, M. Non-destructive local degradation detection in large format lithium-ion battery cells using reversible strain heterogeneity. *J. Energy Storage* **2021**, *40*, 102788. [CrossRef]
3. Bandhauer, T.M.; Garimella, S.; Fuller, T.F. A Critical Review of Thermal Issues in Lithium-Ion Batteries. *J. Electrochem. Soc.* **2011**, *158*, R1. [CrossRef]
4. Gao, Y.; Jiang, J.; Zhang, C.; Zhang, W.; Ma, Z.; Jiang, Y. Lithium-ion battery aging mechanisms and life model under different charging stresses. *J. Power Sources* **2017**, *356*, 103–114. [CrossRef]
5. Attia, P.M.; Moch, E.; Herring, P.K. Challenges and opportunities for high-quality battery production at scale. *Nat. Commun.* **2025**, *16*, 611. [CrossRef] [PubMed]
6. Friedrich, S.; Helmer, S.; Reuter, L.; Dickmanns, J.L.S.; Durdel, A.; Jossen, A. Effect of Mechanical Pressure on Rate Capability, Lifetime, and Expansion in Multilayer Pouch Cells with Silicon-Dominant Anodes. *J. Electrochem. Soc.* **2024**, *171*, 090503. [CrossRef]
7. Deich, T.; Storch, M.; Steiner, K.; Bund, A. Effects of module stiffness and initial compression on lithium-ion cell aging. *J. Power Sources* **2021**, *506*, 230163. [CrossRef]
8. Hahn, S.; Theil, S.; Kroggel, J.; Birke, K.P. Pressure Prediction Modeling and Validation for Lithium-Ion Pouch Cells in Buffered Module Assemblies. *J. Energy Storage* **2021**, *40*, 102517. [CrossRef]
9. Meidiono, R.; Reddy, A.B.; Schieder, M.; Abbasi, F. Evaluation of the mechanical properties evolution of battery pads due to charging-discharging cycles in prismatic Li-ion battery cells. *Proc. Inst. Mech. Eng. Part C J. Mech. Eng. Sci.* **2025**, *239*, 8760–8769. [CrossRef]
10. Zhong, X.; Yang, L.; Li, N.; Chu, Z.; Chen, J.; Zhu, S.; Song, W.L.; Ai, S.; Chen, H.S. In-situ characterizations and mechanism analysis of mechanical inhomogeneity in a prismatic battery module. *J. Power Sources* **2022**, *548*, 232053. [CrossRef]
11. Lokhande, P.E.; Misal, P.; Kalubarme, R.S.; Kulkarni, M.V.; Rednam, U.; Padlkar, S.; Al-Asbahi, B.A. Scalable microwave-assisted production of Ti_3C_2Tx MXene for next-generation Li-ion and Na-ion batteries. *Diam. Relat. Mater.* **2025**, *157*, 112503. [CrossRef]
12. Lokhande, P.E.; Pakdel, A.; Pathan, H.M.; Kumar, D.; Vo, D.V.N.; Al-Gheethi, A.; Sharma, A.; Goel, S.; Singh, P.P.; Lee, B.K. Prospects of MXenes in energy storage applications. *Chemosphere* **2022**, *297*, 134225. [CrossRef] [PubMed]
13. BhaskaraRao, B.V.; Pabba, D.P.; Aepuru, R.; Akbari-Fakhrabadi, A.; Lokhande, P.; Udayabhaskar, R.; Rosales-Vera, M.; Espinoza-González, R. Fe3O4 nanoparticles intercalated reduced graphene oxide nanosheets for supercapacitor and lithium-ion battery anode performance. *J. Mater. Sci. Mater. Electron.* **2023**, *34*, 1910. [CrossRef]
14. Vanem, E.; Salucci, C.B.; Bakdi, A.; sheim Alnes, Ø.Å. Data-driven state of health modelling—A review of state of the art and reflections on applications for maritime battery systems. *J. Energy Storage* **2021**, *43*, 103158. [CrossRef]
15. Zhu, J.; Wang, Y.; Huang, Y.; Bhushan Gopaluni, R.; Cao, Y.; Heere, M.; Mühlbauer, M.J.; Mereacre, L.; Dai, H.; Liu, X.; et al. Data-driven capacity estimation of commercial lithium-ion batteries from voltage relaxation. *Nat. Commun.* **2022**, *13*, 2261. [CrossRef]
16. Zhang, M.; Yang, D.; Du, J.; Sun, H.; Li, L.; Wang, L.; Wang, K. A Review of SOH Prediction of Li-Ion Batteries Based on Data-Driven Algorithms. *Energies* **2023**, *16*, 3167. [CrossRef]
17. Ren, Z.; Du, C.; Zhao, Y.; Ren, Z.; Du, C.; Zhao, Y. A Novel Method for State of Health Estimation of Lithium-Ion Batteries Based on Deep Learning Neural Network and Transfer Learning. *Batteries* **2023**, *9*, 585. [CrossRef]

18. Deng, Y.; Du, C.; Ren, Z.; Deng, Y.; Du, C.; Ren, Z. A Novel Method for Estimating the State of Health of Lithium-Ion Batteries Based on Physics-Informed Neural Network. *Batteries* **2025**, *11*, 49. [CrossRef]
19. Ai, W.; Wu, B.; Martínez-Pañeda, E. A coupled phase field formulation for modelling fatigue cracking in lithium-ion battery electrode particles. *J. Power Sources* **2022**, *544*, 231805. [CrossRef]
20. Mukhopadhyay, A.; Sheldon, B.W. Deformation and stress in electrode materials for Li-ion batteries. *Prog. Mater. Sci.* **2014**, *63*, 58–116. [CrossRef]
21. Nagda, V.; Ekström, H.; Kulachenko, A. Impact of Mechanical Degradation in Polycrystalline NMC Particle on the Electrochemical Performance of Lithium-Ion Batteries. *J. Electrochem. Soc.* **2024**, *171*, 060526. [CrossRef]
22. Lundkvist, A.; Larsson, P.L.; Iyer, A.H.S.; Olsson, E. Discrete element modelling of the elastic-plastic and viscoelastic properties of a lithium-ion battery electrode layer. *Powder Technol.* **2024**, *443*, 119873. [CrossRef]
23. Trembacki, B.L.; Noble, D.R.; Ferraro, M.E.; Roberts, S.A. Mesoscale Effects of Composition and Calendering in Lithium-Ion Battery Composite Electrodes. *J. Electrochem. Energy Convers. Storage* **2020**, *17*, 041001. [CrossRef]
24. Gupta, P.; Gudmundson, P. Modeling of local electrode stresses and pressures in lithium-ion battery packs using three-dimensional homogenization. *J. Power Sources* **2023**, *582*, 233514. [CrossRef]
25. Zhang, W.J. A review of the electrochemical performance of alloy anodes for lithium-ion batteries. *J. Power Sources* **2011**, *196*, 13–24. [CrossRef]
26. Jiang, Z.; Li, J.; Yang, Y.; Mu, L.; Wei, C.; Yu, X.; Pianetta, P.; Zhao, K.; Cloetens, P.; Lin, F.; et al. Machine-learning-revealed statistics of the particle-carbon/binder detachment in lithium-ion battery cathodes. *Nat. Commun.* **2020**, *11*, 2310. [CrossRef]
27. Wu, H.; Xie, Z.; Wang, Y.; Lu, C.; Ma, Z. Modeling diffusion–induced stress on two-phase lithiation in lithium-ion batteries. *Eur. J. Mech.-A/Solids* **2018**, *71*, 320–325. [CrossRef]
28. Zhao, Y.; Xu, B.X.; Stein, P.; Gross, D. Phase-field study of electrochemical reactions at exterior and interior interfaces in Li-ion battery electrode particles. *Comput. Methods Appl. Mech. Eng.* **2016**, *312*, 428–446. [CrossRef]
29. Zhu, X.; Chen, H.; Luan, W. On the study of cyclic plasticity behaviour of primary electrode particle for lithium-ion battery. *Eur. J. Mech.-A/Solids* **2021**, *86*, 104175. [CrossRef]
30. Li, R.; Ren, D.; Guo, D.; Xu, C.; Fan, X.; Hou, Z.; Lu, L.; Feng, X.; Han, X.; Ouyang, M. Volume Deformation of Large-Format Lithium Ion Batteries under Different Degradation Paths. *J. Electrochem. Soc.* **2019**, *166*, A4106. [CrossRef]
31. Cannarella, J.; Arnold, C.B. Stress evolution and capacity fade in constrained lithium-ion pouch cells. *J. Power Sources* **2014**, *245*, 745–751. [CrossRef]
32. Aufschläger, A.; Durdel, A.; Kraft, L.; Jossen, A. Optimizing mechanical compression for cycle life and irreversible swelling of high energy and high power lithium-ion pouch cells. *J. Energy Storage* **2024**, *76*, 109883. [CrossRef]
33. Barai, A.; Tangirala, R.; Uddin, K.; Chevalier, J.; Guo, Y.; McGordon, A.; Jennings, P. The effect of external compressive loads on the cycle lifetime of lithium-ion pouch cells. *J. Energy Storage* **2017**, *13*, 211–219. [CrossRef]
34. Jin, C.; Wang, Y.; Borujerdi, A.S.; Li, J. Stress evolution and thickness change of a lithium-ion pouch cell under various cycling conditions. *J. Power Sources Adv.* **2022**, *16*, 100103. [CrossRef]
35. Liu, D.; Wang, Y.; Xie, Y.; He, L.; Chen, J.; Wu, K.; Xu, R.; Gao, Y. On the stress characteristics of graphite anode in commercial pouch lithium-ion battery. *J. Power Sources* **2013**, *232*, 29–33. [CrossRef]
36. Mohtat, P.; Lee, S.; Siegel, J.B.; Stefanopoulou, A.G. Reversible and Irreversible Expansion of Lithium-Ion Batteries Under a Wide Range of Stress Factors. *J. Electrochem. Soc.* **2021**, *168*, 100520. [CrossRef]
37. Avdyli, A.; von Kessel, O.; Birke, K.P.; Fill, A. Differentiating the effects of pressure in NMC-graphite lithium-ion batteries on cell and system level. *Future Batter.* **2025**, *8*, 100120. [CrossRef]
38. De Sutter, L.; Berckmans, G.; Marinaro, M.; Wohlfahrt-Mehrens, M.; Berecibar, M.; Van Mierlo, J. Mechanical behavior of Silicon-Graphite pouch cells under external compressive load: Implications and opportunities for battery pack design. *J. Power Sources* **2020**, *451*, 227774. [CrossRef]
39. Louli, A.J.; Ellis, L.D.; Dahn, J.R. Operando Pressure Measurements Reveal Solid Electrolyte Interphase Growth to Rank Li-Ion Cell Performance. *Joule* **2019**, *3*, 745–761. [CrossRef]
40. Niu, S.; Zhu, G.; Xu, J.; Qu, Q.; Wu, K.; Zheng, H. Analysis on the effect of external press force on the performance of LiNi0.8Co0.1Mn0.1O2/Graphite large pouch cells. *J. Energy Storage* **2021**, *44*, 103425. [CrossRef]
41. Michelini, E.; Höschele, P.; Heindl, S.F.; Erker, S.; Ellersdorfer, C. Experimental Investigation on Reversible Swelling Mechanisms of Lithium-Ion Batteries under a Varying Preload Force. *Batteries* **2023**, *9*, 218. [CrossRef]
42. Wünsch, M.; Kaufman, J.; Sauer, D.U. Investigation of the influence of different bracing of automotive pouch cells on cyclic liefetime and impedance spectra. *J. Energy Storage* **2019**, *21*, 149–155. [CrossRef]
43. Clerici, D.; Mocera, F.; Somà, A. Electrochemical–mechanical multi-scale model and validation with thickness change measurements in prismatic lithium-ion batteries. *J. Power Sources* **2022**, *542*, 231735. [CrossRef]
44. Mohan, S.; Kim, Y.; Siegel, J.B.; Samad, N.A.; Stefanopoulou, A.G. A Phenomenological Model of Bulk Force in a Li-Ion Battery Pack and Its Application to State of Charge Estimation. *J. Electrochem. Soc.* **2014**, *161*, A2222–A2231. [CrossRef]

45. Oh, K.Y.; Samad, N.A.; Kim, Y.; Siegel, J.B.; Stefanopoulou, A.G.; Epureanu, B.I. A novel phenomenological multi-physics model of Li-ion battery cells. *J. Power Sources* **2016**, *326*, 447–458. [CrossRef]
46. Sauerteig, D.; Hanselmann, N.; Arzberger, A.; Reinshagen, H.; Ivanov, S.; Bund, A. Electrochemical-mechanical coupled modeling and parameterization of swelling and ionic transport in lithium-ion batteries. *J. Power Sources* **2018**, *378*, 235–247. [CrossRef]
47. Kong, D.; Fu, L.; Yang, Q.; He, Y.; Hu, H. Revealing the mechanical behaviour and material micro-structure of graphite electrode coatings in lithium-ion batteries during lithiation. *Phys. Chem. Chem. Phys.* **2025**, *27*, 6179–6192. [CrossRef]
48. Gupta, P.; Üçel, İ.B.; Gudmundson, P.; Olsson, E. Characterization of the Constitutive Behavior of a Cathode Active Layer in Lithium-Ion Batteries Using a Bending Test Method. *Exp. Mech.* **2020**, *60*, 847–860. [CrossRef]
49. Üçel, İ.B.; Gupta, P.; Gudmundson, P. Experimental determination of the constitutive properties of a graphite anode layer in lithium-ion batteries using a bending test method. *J. Energy Storage* **2022**, *46*, 103845. [CrossRef]
50. Rydefalk, C.; Hagman, A.; Yang, L.; Kulachenko, A. Mechanical Response of Paperboard in Rapid Compression—The Rapid ZD-Tester, A Measurement Technique. In *Proceedings of the Transactions of the XVIIth Fundamental Research Symposium Cambridge, 2022*; Pulp & Paper Fundamental Research Committee (FRC): Manchester, UK, 2022; pp. 311–331. [CrossRef]
51. von Kessel, O.; Avdyli, A.; Vrankovic, D.; Birke, K.P. Swelling, pressure evolution and aging in high-silicon/ graphite composite lithium-ion batteries. *J. Power Sources* **2024**, *610*, 234582. [CrossRef]
52. Saltelli, A.; Annoni, P.; Azzini, I.; Campolongo, F.; Ratto, M.; Tarantola, S. Variance based sensitivity analysis of model output. Design and estimator for the total sensitivity index. *Comput. Phys. Commun.* **2010**, *181*, 259–270. [CrossRef]
53. Mussa, A.S.; Klett, M.; Lindbergh, G.; Lindström, R.W. Effects of external pressure on the performance and ageing of single-layer lithium-ion pouch cells. *J. Power Sources* **2018**, *385*, 18–26. [CrossRef]

Disclaimer/Publisher's Note: The statements, opinions and data contained in all publications are solely those of the individual author(s) and contributor(s) and not of MDPI and/or the editor(s). MDPI and/or the editor(s) disclaim responsibility for any injury to people or property resulting from any ideas, methods, instructions or products referred to in the content.